Molecular blueprint of allosteric binding sites in a homologue of the agonist-binding domain of the α7 nicotinic acetylcholine receptor

Radovan Spurny[a], Sarah Debaveye[a], Ana Farinha[a], Ken Veys[b], Ann M. Vos[c], Thomas Gossas[d], John Atack[e], Sonia Bertrand[f], Daniel Bertrand[f], U. Helena Danielson[d,g], Gary Tresadern[c], and Chris Ulens[a,1]

[a]Laboratory of Structural Neurobiology, Katholieke Universiteit Leuven, Leuven B-3000, Belgium; [b]Neurosciences and [c]Discovery Sciences, Janssen Research and Development, Beerse B-2340, Belgium; [d]Beactica AB, SE-752 37 Uppsala, Sweden; [e]Translational Drug Discovery Group, University of Sussex, BN1 9QJ Brighton, United Kingdom; [f]HiQscreen,1222 Vésenaz, Geneva, Switzerland; and [g]Department of Chemistry, Uppsala Biomedical Center, Uppsala University, SE-751 23 Uppsala, Sweden

The α7 nicotinic acetylcholine receptor (nAChR) belongs to the family of pentameric ligand-gated ion channels and is involved in fast synaptic signaling. In this study, we take advantage of a recently identified chimera of the extracellular domain of the native α7 nicotinic acetylcholine receptor and acetylcholine binding protein, termed α7-AChBP. This chimeric receptor was used to conduct an innovative fragment-library screening in combination with X-ray crystallography to identify allosteric binding sites. One allosteric site is surface-exposed and is located near the N-terminal α-helix of the extracellular domain. Ligand binding at this site causes a conformational change of the α-helix as the fragment wedges between the α-helix and a loop homologous to the main immunogenic region of the muscle α1 subunit. A second site is located in the vestibule of the receptor, in a preexisting intrasubunit pocket opposite the agonist binding site and corresponds to a previously identified site involved in positive allosteric modulation of the bacterial homolog ELIC. A third site is located at a pocket right below the agonist binding site. Using electrophysiological recordings on the human α7 nAChR we demonstrate that the identified fragments, which bind at these sites, can modulate receptor activation. This work presents a structural framework for different allosteric binding sites in the α7 nAChR and paves the way for future development of novel allosteric modulators with therapeutic potential.

ligand-gated ion channel | Cys-loop receptor | X-ray crystallography | fragment screen | allosteric modulator

Nicotinic acetylcholine receptors (nAChRs) belong to the class of pentameric ligand-gated ion channels or Cys-loop receptors, which play a crucial role in fast synaptic signaling in the central and peripheral nervous system (1, 2). nAChRs are specifically activated by the endogenous neurotransmitter acetylcholine, which binds to a ligand-binding site in the extracellular domain of the receptor and triggers opening of a channel gate located downstream in the transmembrane domain. This results in a flux of cations through the channel pore, which depolarizes the cell membrane and initiates the action potential. Together with serotonin 5-HT$_3$ receptors, nAChRs belong to the category of excitatory ligand-gated ion channels. In contrast, glycine and γ-aminobutyric acid (GABA$_{A/C}$) receptors form anion-selective pores and belong to the category of inhibitory ligand-gated ion channels. Cys-loop receptors are mutated in a diverse range of inherited neurological disorders, including epilepsy, myasthenia gravis, and hyperekplexia. Additionally, Cys-loop receptors form the target for a wide variety of therapeutically used drugs, including benzodiazepines, barbiturates, general anesthetics, and anthelmintics (3–5). Important to note is that most of these drugs exert their effect by binding to an allosteric site that is remote from the agonist binding site of the receptor.

Most of the high-resolution structural information on nicotinic receptors derives from molluscan acetylcholine binding proteins (AChBPs), which are homologous to the large extracellular ligand-binding domain of nAChRs but lack a pore-forming transmembrane

domain (3, 6–9). The architecture of the complete *Torpedo* nAChR ion channel is shown in Fig. 1*A*, displaying the extracellular, transmembrane, and intracellular domains. AChBPs assemble as homopentamers and have an architectural fold that closely resembles the ligand-binding domain of Cys-loop receptors, including the invertebrate glutamate-gated chloride channel GluCl (10, 11), as well as the bacterial homologs GLIC (8, 12, 13) and ELIC (8, 14). The pharmacological properties of AChBPs are mostly similar to the neuronal α7 subtype of nicotinic receptors (8, 10, 15, 16), which also function as homopentamers. To date, more than 70 cocrystal structures of AChBPs in complex with different agonists, partial agonists, and antagonists have been determined. These studies have revealed a wealth of information on the structural determinants of ligand recognition and the conformational changes occurring during ligand binding. The orthosteric ligand-binding site is located at the interface between a "principal" and "complementary" subunit and is lined by several highly conserved aromatic residues located on three loops in each subunit, termed loops A, B, and C on the principal face and loops D, E, and F on the complementary face. Ligand binding triggers conformational changes in the ligand-binding site, which couple to

Significance

In this study we take advantage of a recently described chimera of the α7 nicotinic acetylcholine receptor (nAChR) and acetylcholine binding protein (AChBP), termed α7-AChBP. To date, more than 70 crystal structures have been determined for AChBP in complex with ligands that occupy the orthosteric binding site. Here, we use an innovative screening strategy to discover molecular fragments that occupy allosteric binding sites. In combination with X-ray crystallography we determine a molecular blueprint of three different allosteric sites in α7-AChBP. Using electrophysiological recordings on the human α7 nAChR we demonstrate that each of the three sites is involved in allosteric modulation of the receptor. Our study contributes to understanding the sites of allosteric binding in ion channels.

Fig. 1. Structure of α7-AChBP and location of the agonist binding site. (*A*) Side view of the *Torpedo* nAChR (PDB ID code 2BG9) in cartoon representation. Different colors are used for extracellular domain (ECD, blue), transmembrane domain (TMD, red) and intracellular domain (ICD, green). (*B*) Top-down view of the α7-AChBP crystal structure in complex with lobeline. Each subunit of the pentamer is shown in a different color. (*C*) Detailed side view of the agonist binding site in α7-AChBP, which is localized at the subunit interface of the (+) and (−) subunit. Lobeline is shown in yellow sphere representation. The α7-AChBP chimera is shown in cartoon representation and blue regions correspond to residues originating from the α7 nAChR (UniProt accession code P36544), whereas orange regions correspond to residues from *Lymnaea* AChBP (UniProt accession code P58154). (*D* and *E*) Detailed view of the agonist binding site, highlighting the different binding pose of lobeline in the α7-AChBP structure (*D*) and the *Aplysia* AChBP structure (*E*). The conserved aromatic residues of the agonist binding site are shown in ball and stick representation. The blue circles indicate the corresponding "loops" of the binding site, termed loops A, B, and C on the (+) subunit and loop D on the (−) subunit. In α7-AChBP, lobeline pinches onto W53 (loop D), whereas in *Aplysia* AChBP lobeline adopts an extended binding mode. The dashed line indicates a hydrogen bond.

channel opening. Despite these insights, structural data on ligand recognition are currently limited to ligands binding in the orthosteric or agonist binding site of nicotinic receptors, whereas information on allosteric binding sites is lacking. Detailed structural knowledge of possible allosteric binding sites in nicotinic receptors is fundamentally important and has great therapeutic potential for the development of allosteric modulators. This is especially clear

in the context of benzodiazepines, which bind at allosteric binding sites of the extracellular domain of the GABA$_A$ receptors and are widely prescribed as hypnotics, sedatives, anxiolytics, antiepileptics, and muscle relaxants (17, 18). Positive allosteric modulators (PAMs) of the α7 nAChR are also recognized as having therapeutic potential. Two different types are distinguished based on the functional effect: type I PAMs, for example NS-1738 (17, 19), mainly potentiate the peak current response evoked by the agonist ACh, whereas type II PAMs, for example PNU-120596 (20, 21), both potentiate the peak current response and alter the time course (4, 20). Based on the results of chimeric protein domain fusion experiments distinct allosteric binding sites are expected: Type I PAMs bind at a site in the extracellular domain, whereas type II PAMs bind at a site in the transmembrane domain (20, 22). However, structural data on the molecular determinants of PAM recognition are currently lacking.

In this study, we took advantage of a recently established α7-nicotinic receptor chimera constructed from the human α7 ligand-binding domain and AChBP (20, 23). This receptor, termed α7-AChBP, shares 71% sequence similarity with the native α7 receptor, including surface-exposed pockets and loops. This is much improved compared with the similarity of 33% between the widely used *Aplysia* AChBP and the human sequence. Our results show that small amino acid differences result in a different ligand-binding orientation for lobeline, a result critical when performing structure-based drug design. To bias our search toward allosteric binders we used a surface plasmon resonance (SPR)-biosensor-based fragment screening approach in which the orthosteric binding site of α7-AChBP was blocked. This was achieved using two different strategies that were applied in parallel during the screen. The first strategy was to block the orthosteric binding site by preincubation with a high-affinity ligand. The second strategy was to use competition in solution where each fragment was mixed with an orthosteric ligand of lower affinity. This allowed detection of fragments not competing for binding to the orthosteric site and were therefore potential allosteric ligands. Multiple allosteric binders were identified and X-ray crystal structures of α7-AChBP in complex with these fragments are reported herein. These structures reveal three novel allosteric binding sites in the α7 extracellular domain. In combination with electrophysiological recordings on the human α7 nAChR we demonstrate that fragment binding at these sites modulates receptor function. Altogether, the results reveal a molecular blueprint of novel binding sites in the α7 nAChR. This work paves the way for future development of novel positive allosteric modulators of the α7 nAChR, which is intensively studied as a potential target to improve cognitive impairment in certain disease states, including Alzheimer's disease (1, 24).

Results

The Agonist Binding Site in α7-AChBP. Before describing the screening we first present our X-ray crystallographic results describing the binding of lobeline at the orthosteric site in α7 nAChR. AChBPs have been highly instrumental in structural studies aimed at revealing ligand-bound nicotinic receptor complexes. However, these studies have been limited to ligands acting at the orthosteric agonist binding site of nicotinic receptors. Currently, more than 70 crystal structures of AChBPs in complex with different orthosteric ligands have been determined (3, 5, 25), most of which were obtained from different crystal forms and different crystallization conditions. The quality of crystal diffraction and the resolution of the X-ray data varies widely, from 4.2 Å for the α-cobratoxin complex with *Lymnaea* AChBP (6, 25) to 1.75 Å for a DMXBA-analog in complex with *Aplysia* AChBP (10, 26). The different crystal forms are largely dependent on the conformation of loop C, which often forms crystal contacts between neighboring pentamers in the crystal packing and is strongly influenced by the nature of the ligand in the agonist binding site. To facilitate our structural studies of allosteric binders with

α7-AChBP, we first screened for optimal crystal diffraction of α7-AChBP with a ligand preoccupying the orthosteric site. From this screen, we found that crystals of α7-AChBP in complex with lobeline gave high diffraction quality in a reproducible manner. The diffraction limit for the different complexes with allosteric binders plus lobeline ranges from 2.1 to 2.8 Å (crystallographic statistics are reported in Table 1). Fig. 1 *B* and *C* shows a cartoon representation of α7-AChBP in complex with lobeline, which has the expected pentameric architecture with five subunits radially assembled around the vestibule-lining axis. The orthosteric binding site is located at the interface between each of two subunits and lobeline is shown in sphere presentation (Fig. 1*C*). Unexpectedly, we observe that lobeline adopts a binding pose in α7-AChBP that is different from the one previously reported in the *Aplysia* or *Capitella* AChBP complexes (8, 27) (Fig. 1 *D* and *E*). In α7-AChBP, lobeline adopts a tweezer-like conformation (Fig. 1*D*) with the two aromatic rings pinching onto the highly conserved aromatic residue of loop D (W53 in α7-AChBP). Here, lobeline forms intramolecular interactions between the hydrogen on the protonated piperidine nitrogen and its own alcohol and carbonyl functional groups. In contrast, in the *Aplysia* and *Capitella* AChBP complexes, lobeline adopts an extended conformation (Fig. 1*E*), which favors interactions with both faces of the subunit interface. Specifically, the extended conformation is mediated by a hydrogen bond between the central piperidine nitrogen and the carbonyl oxygen of the highly conserved aromatic residue of loop B (W145 in *Aplysia* AChBP) (8, 28), which is an interaction not present in the α7-AChBP complex despite a similar spatial position of this tryptophan. In α7-AChBP, lobeline pinches onto W53 and this interaction seems important. In comparison, *Aplysia* AChBP and *Capitella* AChBP contain Y53 and I64, respectively, which likely prevent a pinching binding pose of lobeline. Importantly, W53 is highly conserved between the α7 nAChR and other nicotinic ACh receptors. Therefore, it is likely that our crystallographic binding pose in α7-AChBP is a more realistic model for understanding ligand recognition in the native nAChRs. Nevertheless, these distinct binding orientations of lobeline in different AChBP complexes highlight the plasticity of the binding pocket, which can accommodate ligands in different binding modes despite similar arrangement of highly conserved aromatic residues.
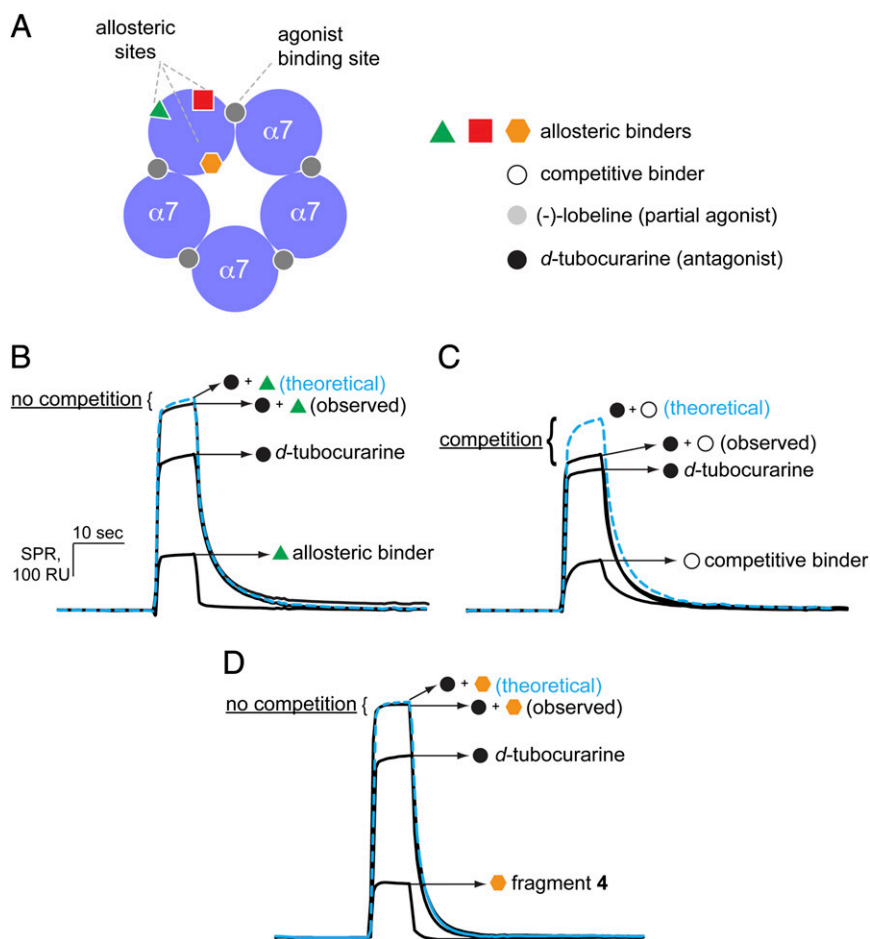
Three Allosteric Binding Sites in α7-AChBP. We performed a fragment-based screen and designed a strategy to identify novel allosteric binding sites using SPR spectroscopy (Fig. 2*A*). In short,

Table 1. Crystallographic data

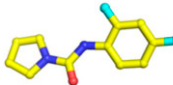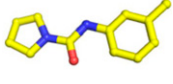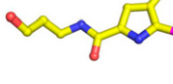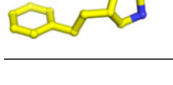| Statistics	α7-AChBP + lobeline	α7-AChBP + lobeline + fragment 1	α7-AChBP + lobeline + fragment 2	α7-AChBP + lobeline + fragment 3	α7-AChBP + lobeline + fragment 4	α7-AChBP + lobeline + fragment 5
Crystallographic statistics						
Beamline	PROXIMA 1 (SOLEIL)	PX-III (SLS)	PROXIMA 1 (SOLEIL)	PROXIMA 1 (SOLEIL)	ID23-2 (ESRF)	ID23-2 (ESRF)
Date of collection	May 21, 2014	Nov. 10, 2012	Apr. 2, 2013	Apr. 2, 2013	Nov. 30, 2013	Nov. 30, 2013
Wavelength, Å	0.9194	0.9194	0.98011	0.98011	0.9194	0.9194
Spacegroup	$P2_12_12_1$	$P2_12_12_1$	$P2_12_12_1$	$P2_12_12_1$	$P2_12_12_1$	$P2_12_12_1$
a,b,c, Å	85.52, 112.50, 143.11	85.20, 106.47, 140.99	85.93, 112.24, 144.70	85.80, 112.29, 143.72	75.77, 119.69, 143.35	86.93, 112.16, 144.68
α, β, γ, °	90.0, 90.0, 90.0	90.0, 90.0, 90.0	90.0, 90.0, 90.0	90.0, 90.0, 90.0	90.0, 90.0, 90.0	90.0, 90.0, 90.0
Resolution limits, Å	49.32–2.40 (2.53–2.40)	48.38–2.22 (2.34–2.22)	48.23–2.46 (2.59–2.46)	47.91–2.35 (2.48–2.35)	47.78–2.78 (2.93–2.78)	47.12–2.22 (2.32–2.22)
R_{merge}, %	7.0 (86.1)	5.9 (83.8)	7.0 (123.3)	7.7 (120.2)	8.6 (91.5)	8.9 (146.8)
$<I/\sigma>$	14.2 (1.5)	12.2 (1.5)	17.0 (1.5)	15.8 (1.5)	11.0 (1.5)	14.3 (1.5)
Resolution at $<I/\sigma>$ 2.0	2.51	2.35	2.58	2.50	2.90	2.54
$CC_{1/2}$	0.998 (0.656)	0.999 (0.564)	0.999 (0.637)	0.999 (0.622)	0.998 (0.709)	0.999 (0.619)
Multiplicity	4.4 (3.9)	3.4 (3.4)	5.9 (6.0)	5.9 (6.0)	4.4 (4.6)	7.5 (7.6)
Completeness, %	99.8 (99.6)	98.8 (99.5)	99.7 (100.0)	99.8 (100.0)	99.9 (99.9)	99.9 (99.7)
Total no. of reflections	239,674 (30,470)	212,558 (31,566)	303,740 (44,856)	345,201 (50,966)	148,336 (21,945)	529,232 (77,193)
No. of unique reflections	54,564 (7,843)	63,044 (9,172)	51,354 (7,427)	58,398 (8,437)	33,519 (4,815)	70,473 (10,143)
Anomalous completeness		89.0 (91.0)			96.6 (98.5)	
Anomalous multiplicity		1.8 (1.8)			2.3 (2.3)	
Refinement statistics						
R_{work}, %	16.80	16.84	16.68	17.08	16.14	16.71
R_{free}, %	22.72	23.29	23.00	23.10	21.72	21.31
Rmsd bond distance, Å	0.009	0.012	0.008	0.007	0.01	0.007
Rmsd bond angle, °	1.229	1.57	1.2	1.123	1.28	1.139
Ramachandran analysis						
Outliers, %	0.3	0.7	0.5	0.5	2.3	0.2
Favored, %	97.13	97.08	96.7	98.1	92.2	98.3
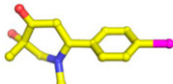
our strategy was to inject each fragment either alone or together with *d*-tubocurarine, which acts as a competitive antagonist at the orthosteric binding site. Our choice of *d*-tubocurarine was based on a thorough evaluation of multiple orthosteric ligands. SPR validation work compared the sensograms and saturation curves for acetylcholine, carbamylcholine, strychnine, tubocurarine, lobeline, nicotine, and α-bungarotoxin. The interactions were studied for the target protein, α7-AChBP, as well as *Capitella* AChBP, which was used as a similar control protein to ensure screening hits would be selective for α7-AChBP and avoid non-specific binders. α-Bungarotoxin was shown to be a slowly dissociating ligand for α7-AChBP that could be used to block the orthosteric binding site. The results showed that *d*-tubocurarine had a fast dissociation rate and could be used as a positive control and as a competitor, providing a high-quality screening assay with Z′ of 0.88 for α7-AChBP and 0.70 for *Capitella* AChBP while allowing for a competition in solution analysis of fragment binding (Z′ is a statistical measure of the screening window, i.e., difference in signal from background, ranging from 0 to 1, with 1 being the theoretical maximum) (29). Although lobeline had a subnanomolar affinity for *Capitella* AChBP, the dissociation rate was not slow enough to allow lobeline to be used as a blocking

agent for the control protein *Capitella* AChBP. Thus, within our screening strategy for allosteric binders, the observed SPR response of fragment plus *d*-tubocurarine would be very close to the theoretical sum of fragment alone and *d*-tubocurarine alone because both ligands bind to separate sites on the receptor and no competition is expected (Fig. 2*B*). In the case of a competitive binder, the observed response of fragment plus *d*-tubocurarine is much lower than the theoretical sum of fragment alone and *d*-tubocurarine alone because both ligands compete for binding at the same site (Fig. 2*C*). The second strategy was simultaneously applied during the screen by comparing the binding signals of fragments for α7-AChBP with the orthosteric binding site blocked by α-bungarotoxin and nonblocked α7-AChBP. Using this strategy, a single concentration screen of 3,028 fragments was performed and 302 potentially allosteric fragment hits were identified. These were further characterized in concentration-response experiments to estimate affinity and 24 potential allosteric binders were selected for cocrystallization based on affinity, competition, and selectivity over *Capitella* AChBP. Cocrystallization trials for α7-AChBP preoccupied with lobeline and the allosteric ligand were set up if the binder remained soluble at a final concentration of 5–10 mM. Lobeline was chosen for crystallization studies because of the

Fig. 2. Design of fragment-based screen for allosteric binders on α7-AChBP. (*A*) Schematic presentation of the location of the agonist binding site in α7-AChBP as well as possible allosteric binding sites. Competitive binders, the agonist lobeline, and the antagonist *d*-tubocurarine all compete for binding at the agonist binding site, whereas allosteric binders bind at different sites. (*B*) To distinguish allosteric binders from competitive binders using SPR spectroscopy we perfused each fragment alone (green triangle) or in combination with the competitive antagonist *d*-tubocurarine (black circle). In the case of an allosteric binder, the response units observed for the mixture of fragment + *d*-tubocurarine is close to the sum of fragment alone + *d*-tubocurarine alone (blue dashed line). No competition exists because the fragment and *d*-tubocurarine bind at distinct sites. (*C*) In the case of a competitive binder, the response units for the mixture of fragment + *d*-tubocurarine is lower than the sum of fragment alone + *d*-tubocurarine alone because both compounds compete for binding at the same site. (*D*) Example traces for fragment **4**, which was identified as one of the allosteric binders in this study.

Table 2. Summary of fragment structure, International Union of Pure and Applied Chemistry (IUPAC) name, location of binding pocket, and contact residues

Fragment structure	Fragment no.	IUPAC name	Location binding pocket	Contact residues
	1	6-(4-bromophenyl)-3-hydroxy-1,3-dimethyl-2H-pyridin-4-one	Top pocket and agonist subpocket	L6, E9, Y62, L63, Y70, V76 L36, Q37, W53, Y91, N92, I94, K141, I165
	2	N-(2,4-difluorophenyl)pyrrolidine-1-carboxamide	Top pocket	L6, E9, Y62, L63, Y70, V76
	3	N-(m-tolyl)pyrrolidine-1-carboxamide	Top pocket	L6, E9, Y62, L63, Y70, V76
	4	4,5-dibromo-N-(3-hydroxypropyl)-1H-pyrrole-2-carboxamide	Vestibule pocket	F31, L33, F52, L54, L88, P97, L100, P102, I119, Q121, F142
	5	4-(2-phenylethyl)pyrrolidin-2-one	Vestibule pocket	F31, L33, F52, L54, L88, P97, L100, P102, I119, Q121, F142

reproducible crystal growth and good-quality diffraction of crystals. From this crystallization screen, we here report cocrystal structures of α7-AChBP with five different fragments bound (fragments **1**–**5**, Table 2). The other remaining fragments produced either poorly diffracting crystals or no clear density for the fragment could be observed in the electron density map. The experimental SPR traces are shown in Fig. 2D for fragment **4**, showing the lack of competition with d-tubocurarine, indicative of allosteric binding.

First, we took advantage of the bromine atom in fragment **1** to collect anomalous diffraction data, which allowed us to pinpoint the location of the bromine atoms in the electron density map.
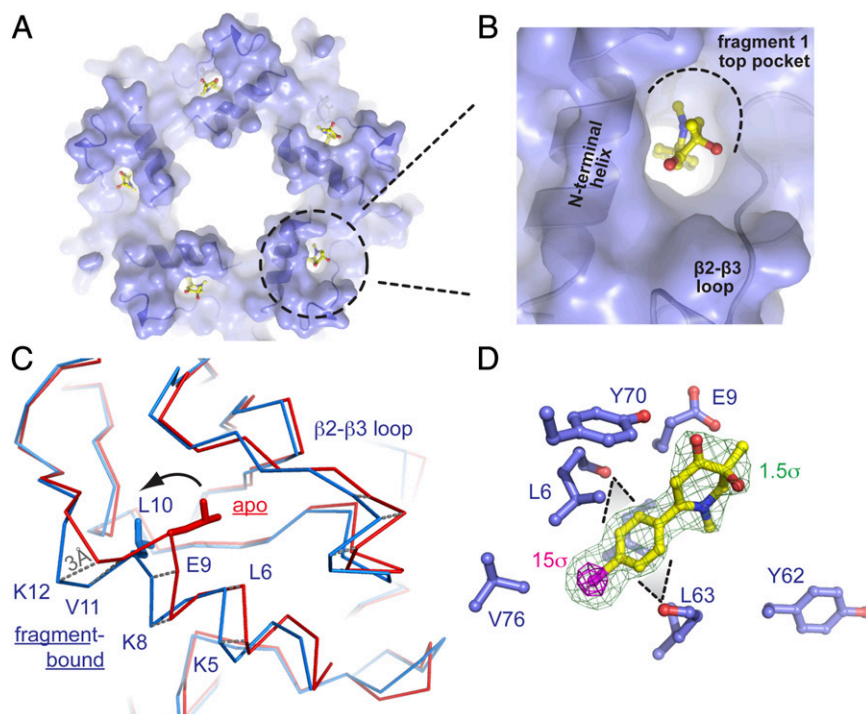
Fig. 3. Allosteric binding at the top pocket in α7-AChBP. (A) Fragment **1** reveals an allosteric binding site located at the N-terminal α-helix of α7-AChBP and is termed the top pocket. α7-AChBP is shown in transparent surface and cartoon representation. Fragment **1** is shown as yellow ball and sticks. (B) Detailed view of fragment **1**, wedging between the N-terminal helix and the β2–β3 loop. (C) Binding of fragment **1** causes a conformational change of the N-terminal helix, which is noticeable as a 3-Å displacement of residue K12 and a change in the rotamer of L10. The blue ribbon represents the fragment-bound conformation, and the red ribbon represent the apo state. (D) Detailed view of the amino acid interactions between fragment **1** and residues of the top pocket. Fragment **1** is shown in ball and sticks. Yellow is carbon, red oxygen, blue nitrogen, bromine magenta. The green mesh is $2F_o − F_c$ density contoured at 1.5σ and the magenta mesh is anomalous difference density contoured at 15σ. The black dashed triangles indicate Van der Waals interactions.

Calculation of anomalous difference density maps reveals intense peaks (5σ) in all five subunits located near the N-terminal α-helix and weaker peaks just below the orthosteric binding site (Fig. S1). We first discuss binding to the N-terminal site. At this location, the anomalous density is visible to a level of 15σ and the contours of fragment **1** are further revealed by the simple electron density map, which allowed us to unambiguously assign the binding pose of the fragment (Fig. 3). Fig. 3 *A* and *B* illustrates how fragment **1** forms a wedge between the N-terminal α-helix and the β2–β3 loop, opening up a pocket which we term the "top pocket." Fig. 3*D* shows the electron density of the fragment in the binding site. Binding of fragment **1** to the top pocket is accompanied by a conformational change in the α-helix (K5 to K12), which moves inward by a distance of ∼3 Å in the direction of the receptor vestibule (Fig. 3*C*). The top pocket is further exposed by a side-chain reorientation of residue L10, causing an induced fit to accommodate fragment **1**. In this orientation, the bromophenyl moiety of the fragment points deep into the top pocket, forming van der Waals interactions with the carbonyl oxygen of L6 and L63 (indicated with dashed lines in Fig. 3*D*). Other interactions include residues L6, E9, Y62, L63, Y70, and V76. In addition to the movement of the α-helix, there is also a reorientation of the loop connecting the β2- and β3-strands. Importantly, this region overlaps with the main immunogenic region in the α1-subunit of the muscle nAChR, which plays an important role in myasthenia gravis.

In addition to anomalous density peaks at the top site, we also observe peaks with weaker intensity, but still clearly visible at 5σ, just below the agonist binding site at all five interfaces (Fig. S1). This result indicates that under the current crystallization conditions, fragment **1** likely binds with lower occupancy at this site compared with the top site. The anomalous density, combined with the simple electron density map ($2F_o − F_c$), allowed us to assign the second binding site for fragment **1** (Fig. 4 *A*–*C*). At this location, which we term the "agonist subpocket," fragment **1** binds just in between loop C and loop F, which are important determinants of ligand recognition (8, 10, 16, 28). Similar to binding at the top site, the bromophenyl moiety points into the pocket and forms interactions with the side chains of residues on the (+) subunit, including N92 and I94 (loop A) and K 141 (loop C), as well as residues on the (−) subunit, including Q35 and L36 (loop F) and I165. Importantly, the agonist subpocket overlaps with a possible binding site for the anesthetic ketamine in a cocrystal structure of the bacterial homolog GLIC (17, 30). Ketamine in GLIC was shown to cause channel inhibition and mutagenesis of residues involved in ketamine recognition demonstrated weaker ketamine binding as well as effects on channel gating, indicating that the binding site is functionally important and may offer an attractive target for development of novel allosteric modulators (11, 17). In our study, we extend these observations and find a binding pose for fragment **1** that strongly resembles that of ketamine bound in GLIC (Fig. S2).

Fragment **1** binds to two allosteric binding sites in α7-AChBP; one is the top pocket and the second is the agonist subpocket. In addition, we identified two other fragments, fragments **2** and **3** (Fig. S3), which also occupy the top pocket. Both of these fragments are comparable in chemical structure to each other and adopt a binding pose that partially overlaps with fragment **1** at the top pocket. However, no electron density could be observed for fragment **2** or **3** at the agonist subpocket, indicating that these fragments bind specifically at the top pocket and not at the agonist subpocket.
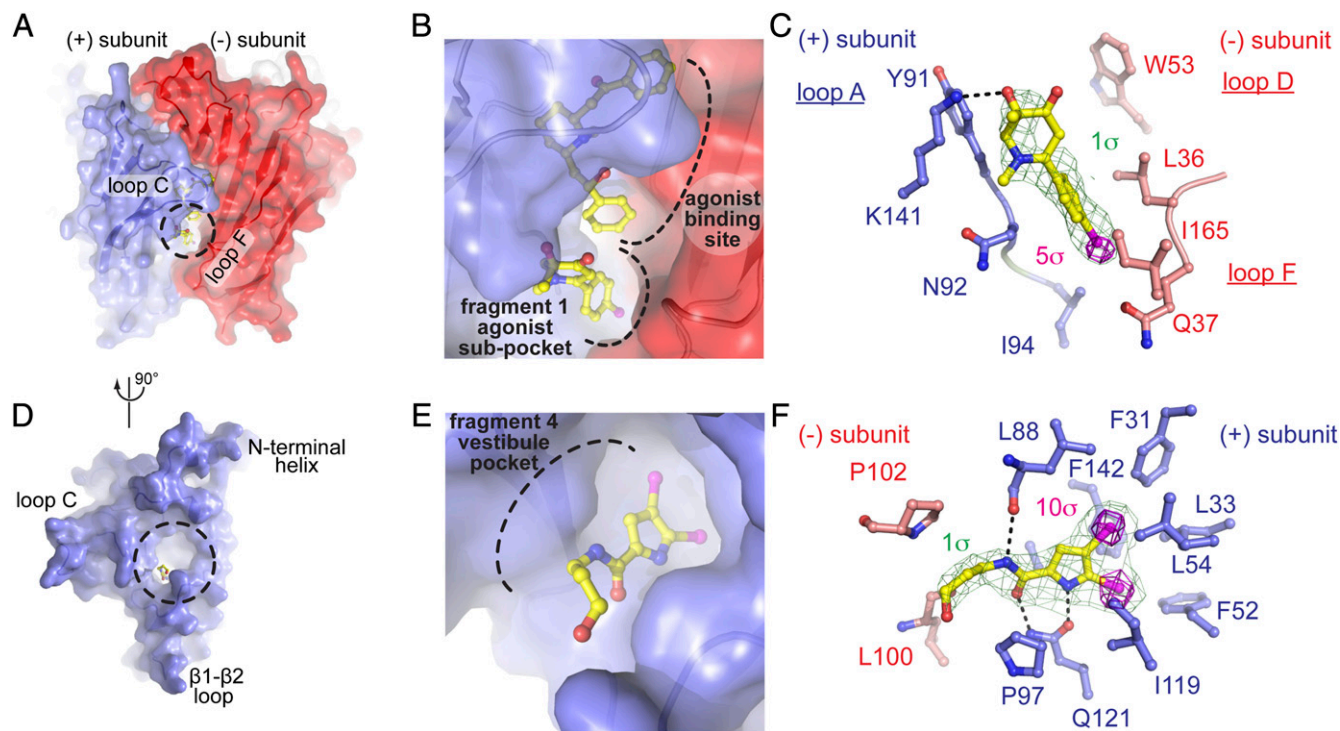
Fig. 4. Allosteric binding at the agonist subpocket and vestibule pocket in α7-AChBP. (*A*) α7-AChBP is shown in transparent surface and cartoon representation. The black dashed circle indicates the location of the agonist subpocket, which is occupied by fragment **1** right below the orthosteric binding site. (*B*) Detailed view of the overlapping agonist binding site and agonist subpocket. Lobeline and fragment **1** are shown in ball and stick presentation. (*C*) Detailed view of the amino acid interactions between fragment **1** and residues of the agonist subpocket. The green mesh is $2F_o − F_c$ density contoured at 1σ and the magenta mesh is anomalous difference density contoured at 5σ. (*D*) The location of the vestibule pocket is indicated with the black dashed circle. (*E*) Detailed view of the vestibule pocket, which is occupied by fragment **4**. (*F*) Detailed view of the amino acid interactions between fragment **4** and residues of the vestibule pocket. The green mesh is $2F_o − F_c$ density contoured at 1σ and the magenta mesh is anomalous difference density contoured at 10σ.

Finally, we again took advantage of the bromine atoms in fragment **4** to collect anomalous diffraction data and map a third distinct binding site in α7-AChBP. For this fragment, calculation of anomalous difference density maps clearly reveals two adjacent peaks (10σ) located in a pocket within each of the five subunits and facing the vestibule of the receptor (Fig. S4). Combined with the simple electron density map ($2F_o − F_c$) we were able to assign the binding pose for fragment **4**, which is illustrated in Fig. 4 *D–F*. At this site, the fragment does not cause any significant conformational changes but rather occupies a preexisting cavity in α7-AChBP, which we term the "vestibule pocket." Similar to fragment **1**, the bromine-containing moiety points into the pocket and forms extensive interactions mainly with residues within one (+) subunit, including F31, L33, F52, L54, P97, I119, and F142. Hydrogen bonds are formed with the backbone carbonyl of L88 and the side-chain atoms of Q121. Two additional interactions are formed with residues of the neighboring (−) subunit and include L100 and P102. Importantly, the vestibule pocket corresponds to a previously identified site in the bacterial homolog ELIC and which is involved in positive allosteric modulation of ELIC by benzodiazepines (20, 31). Cysteine-scanning mutagenesis of residues involved in benzodiazepine recognition at this site in ELIC abolished channel modulation (20, 32). Additionally, modification of certain cysteine residues with (2-((biotinoyl)amino)ethyl methanethiosulfonate) mimicked the effect of benzodiazepines, indicating that occupancy of this pocket mediates positive allosteric modulation. In our study, we confirm the existence of this pocket in α7-AChBP and demonstrate that a fragment with chemical composition different from benzodiazepines can occupy this pocket. This result suggests that compounds with different chemical composition can be designed to specifically target the vestibule pocket in different Cys-loop receptors. The importance of the vestibule pocket and the recognition of chemically diverse compounds at this site are further illustrated by the crystal structure of α7-AChBP in complex with fragment **5** (Fig. S5).
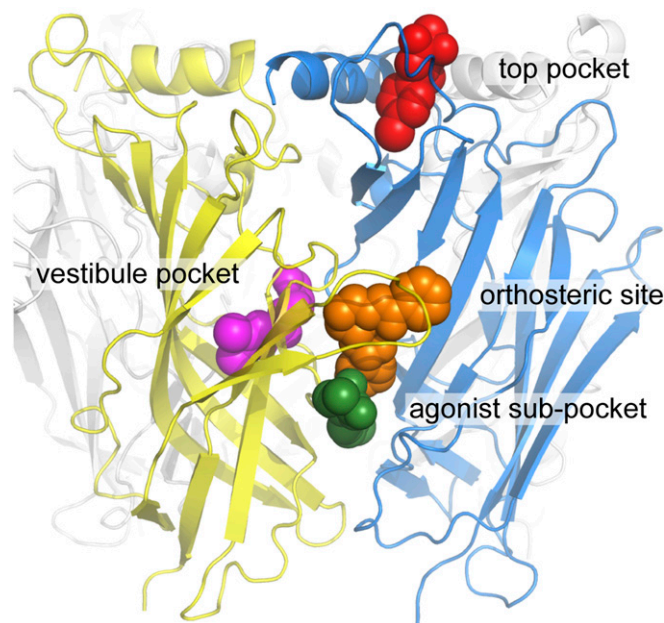
Fig. 5. Overview of the different allosteric binding sites discovered in α7-AChBP. α7-AChBP is shown in cartoon representation. Lobeline and different allosteric binders are presented as spheres. The orange ligand corresponds to lobeline and occupies the orthosteric binding site. The red ligand occupies the top pocket, the green ligand occupies the agonist subpocket, and the magenta ligand occupies the vestibule pocket.

Table 3. Electrophysiological properties of fragments 1–5

	IC$_{50}$, µM	Hill	I$_{max}$, %
Concentration-inhibition curve parameters			
Fragment			
1	42 ± 12	1.27 ± 0.18	
2	132 ± 36	1.08 ± 0.13	
3	398 ± 43	1.21 ± 0.08	
4	70 ± 10	0.87 ± 0.04	
5	34 ± 6	0.77 ± 0.05	
Effect on concentration-activation curve			
Acetylcholine	154 ± 4	1.52 ± 0.01	100
Fragment			
1	215 ± 17	1.36 ± 0.06	42 ± 6
2	215 ± 10	1.57 ± 0.08	54 ± 5
3	216 ± 6	1.58 ± 0.12	42 ± 7
4	126 ± 7	1.66 ± 0.04	48 ± 4
5	179 ± 32	1.56 ± 0.10	47 ± 14

n = 4–7.

In conclusion, five crystal structures of α7-AChBP in complex with different allosteric binders have been described. These fragments were identified by a biophysical SPR screening approach specifically designed to identify allosteric binders. Overall, three allosteric sites were found as summarized in Fig. 5. Fragment **1** binds at two different sites: the top pocket, which was not identified before, and the subagonist pocket, which corresponds to the ketamine binding site in GLIC. Fragments **2** and **3** specifically bind at the top pocket. Fragments **4** and **5** bind at the vestibule pocket, which corresponds to the site involved in positive allosteric modulation of ELIC by benzodiazepines (17, 20). The sequence conservation between the α7 nAChR and *Lymnaea* AChBP at these sites is illustrated in Fig. S6.

Functional Characterization of Fragment Binding at Allosteric Sites. The cocrystal structures of α7-AChBP in complex with the five different allosteric binders raise an important question about whether these allosteric sites are functionally important in channel gating. Detailed functional characterization of these binders was carried out by using the two-electrode voltage clamp technique on *Xenopus* oocytes expressing the human α7 nAChR. Each fragment was tested in a concentration range according to their relatively low affinity from 3 µM to 3 mM and each concentration was coapplied with 1.3 mM acetylcholine (traces are shown in Fig. S7). We observed that all fragments cause a concentration-dependent inhibition of acetylcholine-induced responses of the α7 nAChR (Fig. 6 *A* and *B*). Fragment **5** was the most potent with an IC$_{50}$ value of 34 ± 6 µM (Table 3). Fragment **3** was the least potent with an IC$_{50}$ value of 398 ± 43 µM (Table 3). Fragment **4** gave a partial inhibitory effect, but the analysis of this fragment was complicated owing to solubility issues at millimolar concentrations.

Next, we investigated the effect of each fragment on the concentration-activation curve of acetylcholine. To accomplish this we coapplied a fixed concentration of fragment (IC$_{50}$ value) with increasing concentrations of acetylcholine. We observed that each fragment caused a decrease of the maximal current response of acetylcholine (Fig. 6*C*), which is indicative of a noncompetitive mechanism of action versus acetylcholine and is consistent with the crystal structures. A detailed overview of the Hill fit is given in Table 3.

Next, we investigated the role of each of the allosteric binding sites in mediating inhibitory responses by the fragments through site-directed mutagenesis. We did not consider the agonist subpocket because this site is targeted only by fragment **1**, which also targets the top pocket. This complicates the interpretation of mutagenesis data, and therefore the agonist subpocket was not
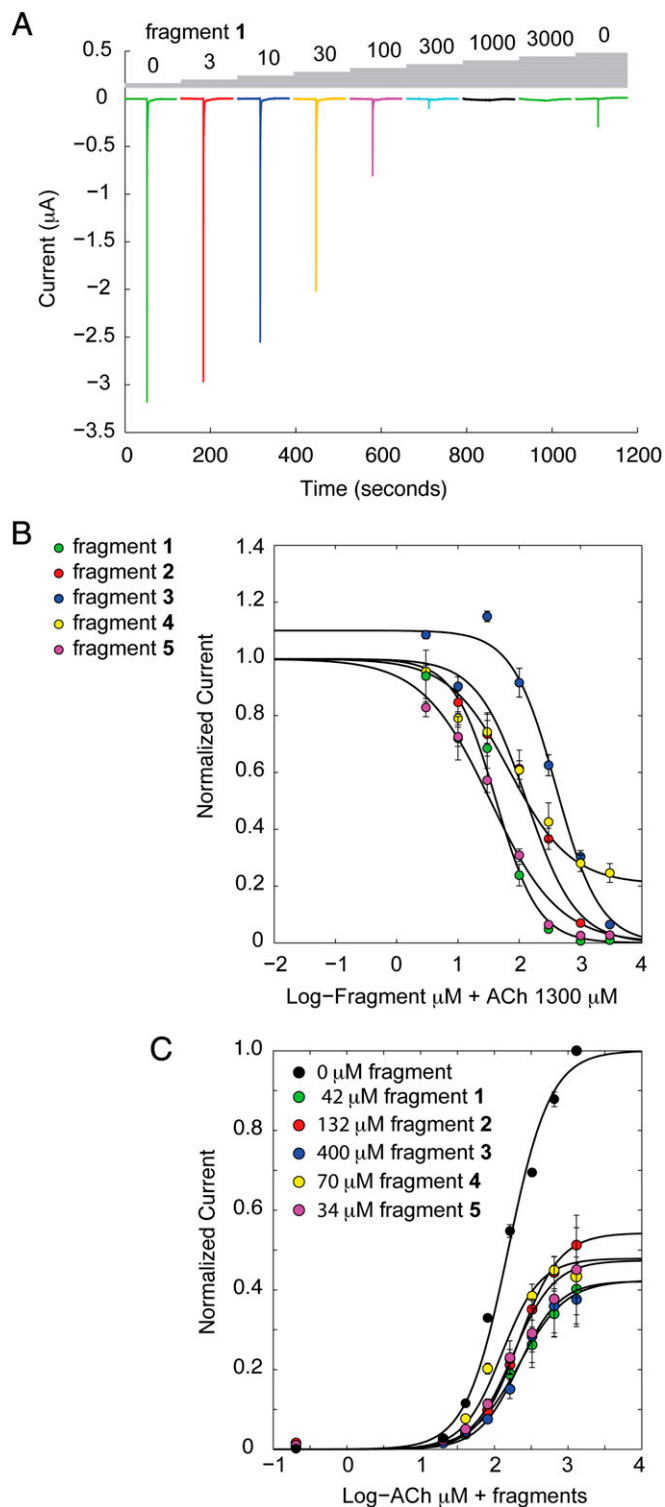
Fig. 6. Functional characterization of allosteric binders on the human α7 nAChR. (A) Example traces of the α7 nAChR repetitively activated with a fixed concentration of acetylcholine (1.3 mM). Coapplication of increasing concentrations of fragment **1** causes a progressive decrease in the ACh-activated current. (B) Concentration-inhibition curves constructed from data shown in A. Error bars indicate SD. (C) Effect of each fragment on the concentration-activation curve of acetylcholine. All of the fragments cause a decrease of the maximal current, without any pronounced effect on the EC$_{50}$ value, which is indicative for an allosteric effect and is consistent with crystal structures.

further investigated. Our mutagenesis approach was to construct phenylalanine mutants at positions in each of the respective pockets that would cause steric hindrance with the fragment. Therefore, we constructed L7F and V78F in the top pocket and L35F and L92F in the vestibule pocket. Double mutants gave responses that were too small for reliable measurements. L92F gave no current responses, indicating this position is structurally important. L7F, V78F, and L35F were functional. Construction of concentration-activation curves for each mutant revealed that L7F and V78F have EC$_{50}$ values for ACh that are not significantly different from WT α7 nAChR (Tables S1 and S2). In contrast, L35F has an EC$_{50}$ value of 81 ± 5 μM compared with 154 ± 4 μM for WT, suggesting this site is functionally important.

The mutagenesis data are most convincing for L35F in the vestibule pocket. Fragments **4** and **5** have IC$_{50}$ values of $2{,}670 \pm 497$ μM and 173 ± 24 μM, respectively, compared with 70 ± 10 μM and 34 ± 6 μM on WT α7 nAChR, which provides strong evidence that the effects of these fragments are mediated through the vestibule pocket. For L7F in the top pocket, we observe that fragment **2** has an IC$_{50}$ value of 229 ± 11 μM compared with 132 ± 36 μM on WT, indicating a possible effect of this fragment through the top pocket. Other values on L7F were not significantly different or even lower than WT (Tables S1 and S2). For V78F in the top pocket, we did not observe significant changes. It should be remembered that site-directed mutagenesis is not without caveats, and the lack of activity difference in this case could be explained if the 78F side chain adopts an alternative rotamer pointing away from the pocket, thereby still allowing binding.

In conclusion, the mutagenesis data provide strong support for an inhibitory action of fragments **4** and **5** through the vestibule pocket and results for one mutant indicate action of fragment **2** through the top pocket.

Together, these data suggest that all of the allosteric binders reported in this study act as negative allosteric modulators on the α7 nAChR. Important to note is that fragments **4** and **5** bind in the vestibule pocket, which is a site involved in positive allosteric modulation of ELIC by benzodiazepines (17, 20). Therefore, we hypothesize that chemical optimization of our fragments, increasing their molecular weight, potency, and number and type of interactions, could lead to a modification in functional activity and cause positive allosteric modulation of the α7 nAChR.

Discussion

Channel opening of the α7 nAChR and other Cys-loop receptors is associated with a conformational transition from a resting nonconductive state to an activated state that opens the channel pore. This transition is typically triggered by binding of an agonist at the orthosteric binding site. Allosteric modulation is defined as the process that modifies the energetic barrier between the resting and activated state and that is caused by binding of a molecule at a site that is different from the orthosteric binding site. PAMs lower the energetic barrier for channel opening and cause potentiation of the evoked current, whereas negative allosteric modulators increase the energetic barrier and inhibit the channel response. From a structural perspective, detailed insight into the molecular determinants of modulator recognition derives from several homologous ion channels, including the prokaryote Cys-loop receptor GLIC and the invertebrate glutamate-gated ion channel GluCl. First, general anesthetics such as desflurane and propofol act as negative allosteric modulators of nAChRs (4, 24), as well as GLIC (4, 25). Cocrystal structures of GLIC with these anesthetics reveal that the binding site for propofol and desflurane is located in the upper part of the transmembrane domain in a preexisting cavity between the M1 and M4 transmembrane helices of each protomer (22, 25). In addition, ethanol acts as a positive allosteric modulator of different ligand-gated ion channels, including nAChRs (23, 26) and GABA$_A$

receptors (27) as well as the ethanol-sensitized F14′A mutant of GLIC (28). The crystal structure of GLIC in complex with ethanol shows that this allosteric binding site is located at an intersubunit transmembrane cavity formed by M1–M2 transmembrane helices of one subunit and M2–M3 transmembrane helices of the neighboring subunit (28). The ethanol binding site overlaps with the binding site for the anthelmintic ivermectin, which is considered as an allosteric agonist of different Cys-loop receptors, including the α7 nAChR (30), and has been cocrystallized with GluCl (11). Next, ketamine is considered as a noncompetitive antagonist of NMDA receptors (31) as well nAChRs (32) and its allosteric binding site has been revealed in a cocrystal structure of GLIC (17). Here, ketamine binds in the extracellular ligand-binding domain at an intersubunit cavity that partially overlaps with the agonist binding site (17) and corresponds to the agonist subpocket described and occupied by our allosteric fragment **1** in this paper. Specifically for the α7 nAChR, positive allosteric modulators are further subdivided into so-called type I and type II modulators (4). Type I PAMs, for example NS-1738, mainly potentiate the peak current response evoked by the agonist ACh, whereas type II PAMs, for example PNU-120596, both potentiate the peak current response and alter the time course (4). Structural data for type I or II PAMs on the α7 nAChR are currently lacking, but a chimeric study has revealed that the binding site for type I PAMs is located in the extracellular domain, whereas the action of type II PAMs relies in part on the M2–M3 loop (22). We note that NS-1738 and our fragments **2** and **3** share a similar and simple linear geometry. A central urea functionality separates two distal monocyclic rings. The close structural similarity prompts speculation whether NS-1738 binds at the same site as **2** and **3**, albeit eliciting the opposite functional effect.

In this study, we have overcome the limitations of distant ion channel homologs such as GLIC and GluCl and carried out a combined fragment screen and structural characterization to identify allosteric binding sites in α7-AChBP, which is a reliable mimic of the extracellular domain of the α7 nAChR (23). We found that allosteric binders can localize to three different sites in the extracellular domain. One allosteric site is surface-exposed and is located near the N-terminal α-helix of the extracellular domain. At this site, allosteric binding causes a conformational change of the α-helix as the fragment wedges between the α-helix and a loop homologous to the main immunogenic region of the muscle α1 subunit. A second site is located in the vestibule of the receptor, in a preexisting intrasubunit pocket opposite the agonist binding site and corresponds to a previously identified site involved in positive allosteric modulation of the bacterial homolog ELIC. A third site is located at a pocket right below the agonist binding site and corresponds to a binding site for the anesthetic ketamine in the bacterial homolog GLIC. It is possible that one of the allosteric sites identified in α7-AChBP in this study corresponds to the allosteric binding site for type I PAMs in the α7 nAChR (22).

In conclusion, this work unveils novel allosteric binding sites in the extracellular domain of the α7 nAChR and paves the way for further development of novel allosteric modulators with therapeutic potential.

Methods

Protein Expression and Crystallization. The α7-AChBP chimera (23) was expressed as a C-terminal Hisx6 fusion using a synthetic gene (Genscript) with optimized codon use for expression in insect cells. The cDNA was cloned into the pFastBac vector and bacmid DNA was produced according to the manufacturer's guidelines of the Bac-to-Bac expression system (Invitrogen). Protein was expressed by addition of baculovirus to a *Spodoptera frugiperda* Sf21 cell culture at a cell density of 1 million cells per milliliter and a multiplicity of infection of around 1. Cell culture medium was harvested 72 h after infection by centrifugation at 10,000 × g and α7-AChBP was purified by incubation of the medium with Ni Sepharose 6 Fast Flow beads (GE Health-

care). Beads were washed with buffer containing 20 mM Tris (pH 8.0), 300 mM NaCl, and 40 mM imidazole. α7-AChBP was eluted with the same buffer containing 300 mM imidazole. A final purification step was carried out using size-exclusion chromatography on a Superdex 200 10/300 GL column (GE Healthcare) in buffer containing 20 mM Tris (pH 8.0) and 300 mM NaCl. Fractions corresponding to pentameric protein were concentrated to 6 mg/mL, snap-frozen in liquid nitrogen, and stored at −80 °C until further use.

For crystallization screening, α7-AChBP was mixed with α-lobeline hydrochloride (Sigma-Aldrich) at a final concentration of 1 mM and fragment at a final concentration of 10 mM. Fragments **1–5** were obtained from commercial compound vendors. The respective CAS numbers were CAS124209-86–5, CAS893019-25–5, CAS35799-26–9, CAS186956-98–9, and CAS206749-62–4. Sitting-drop vapor diffusion crystallization screens were set up using a Mosquito nanoliter crystallization robot (TTP Labtech) and crystal growth was monitored by automated imaging in a Rock Maker (Formulatrix). Crystals grew at 20 °C in the presence of solution composed of 200 mM potassium/sodium tartrate and 20% PEG3350 or 200 mM sodium malonate and 20% PEG3350. Crystals were cryoprotected by addition of 30% (mass/vol) glycerol to the mother liquor and immersed in liquid nitrogen before storage and transportation.

Structure Determination. X-ray diffraction datasets obtained during the course of this study were collected at the PROXIMA-1 beam line of the SOLEIL synchrotron or the PX-III beam line of the Swiss Light Source. Diffraction data were processed with XDS (33) and scaled in Scala of the CCP4 suite (34). Structure solution was obtained using molecular replacement with PHASER or MOLREP (34) and the published α7-AChBP structure (23) as a search model (PDB ID code 3SQ6). Automated structure building was carried out with the Autobuild rebuild in place feature of PHENIX (35). Iterative cycles of structure refinement and manual rebuilding were carried out in PHENIX (35) and Coot (36), respectively. Structure validation was done with Molprobity (37) and figures were prepared in Pymol (Schrödinger).

SPR Screening. A Biacore 4000 instrument (GE Healthcare) was used for fragment screening. The proteins were immobilized on a CM5 chip by amine coupling using standard procedures and materials (GE Healthcare). α7-AChBP was immobilized on spot 4 and spot 5 in all flow cells. *Capitella* AChBP was immobilized on spot 1. (Spot 3 was unmodified and used as reference.) α7-AChBP was prepared as 0.15 mg/mL in 10 mM Hepes, pH 7.0 (Sigma), and injected for 10 min over activated carboxylated dextran surfaces (NHS/EDC). *Capitella* AChBP was prepared as 0.15 mg/mL in 10 mM acetate, pH 5.0 (GE Healthcare), and injected for 10 min over activated carboxylated dextran surfaces (NHS/EDC). The surface was deactivated by 1 M ethanolamine, pH 8.5.

The interaction experiments were performed at 25 °C. PBS (Sigma), with addition of 0.05% Tween 20 (Sigma) and 1% (vol/vol) DMSO (Sigma), was used as assay buffer. Fragments were injected for 15 s at 200 μM using a flow rate of 30 μL/min. All samples were also injected in mixture with 10 μM d-tubocurarine. Negative controls (buffer) and positive controls (10 μM d-tubocurarine and 500 μM acetylcholine) were injected every 40th sample cycle. The orthosteric binding site was blocked by a capture injection of 10 μM α-bungarotoxin (Tocris) every 20th cycle over spot 5 (α7-AChBP). Signals arising from interactions with the sensor surface matrix were removed by subtraction of signals from the unmodified reference surface.

Biacore 4000 evaluation software was used for the analysis of screening data. Report point tables were exported as text files and further calculations were made in Excel (Microsoft).

The degree of competition with d-tubocurarine (DoC_{Tubo}) was calculated using Eq. **1**, where R represents signals not normalized for molecular weight (MW). The signal for the Competitor (R_{Tubo}) was normalized to 100.

$$DoC_{Tubo} = 1 - (R_{Mix} - R_{Tubo})/R_{Fragment}. \quad \text{[1]}$$

The degree of competition with α-bungarotoxin (DoC_{Bunga}) was defined as the relative difference between the scaled signals from the blocked and nonblocked protein using Eq. **2**, where 4.3 represents a scaling factor compensating for the remaining surface activity of the blocked surface.

$$DoC_{Bunga} = (R_{unblocked} - R_{blocked}/4.3)/R_{unblocked}. \quad \text{[2]}$$

The degree of competition with d-tubocurarine (DoC_{Tubo}) was calculated using Eq. **3**, where R represents signals not normalized for MW. The signal for the Competitor (R_{Tubo}) was normalized to 100.

$$DoC_{Tubo} = 100*(1 - (R_{Mix} - R_{Tubo})/R_{Fragment}). \quad \text{[3]}$$

The degree of competition with α-bungarotoxin (DoC_{Bunga}) was defined as the relative difference between the scaled signals from the blocked and

nonblocked protein using Eq. **4**, where SC is a scaling factor ranging between 4 and 5 for different experiments, compensating for the remaining surface activity of the blocked surface.

$$\text{DoC}_{\text{Bunga}} = 100 * (1 - ((R_{\text{blocked}}/\text{SC})/R_{\text{non-blocked}})).$$ **[4]**

Negative values of the DoC were replaced by 0.0 before ranking. Test compounds showing signals less than one-third of the signal from the reference were discarded together with test compounds showing signals more than five times the signal from the reference.

Hits were rank-ordered by use of a multiobjective Pareto ranking as implemented in the Erl Wood community nodes in Knime 2.5.1, based on the MW-normalized responses from the blocked surfaces in combination with the calculated degrees of competition.

The hits from the primary screen were tested in dose–response by injecting the fragments for 15 s at 1.23–300 μM (1:2 dilution series from 300 μM) using a flow rate of 30 μL/min. Samples at 100 μM were also injected in mixture with 10 μM *d*-tubocurarine. Negative controls (buffer) and positive controls (10 μM *d*-tubocurarine) were injected every 24th sample cycle. Furthermore, the orthosteric binding site of α7-AChP immobilized on spot 5 was blocked by a capture injection of 10 μM α-bungarotoxin (Tocris) every 24th cycle over spot 5 (α7-AChBP). Replicate experiments were performed similarly but using a 1.95–500 μM 1:1 dilution series of the fragments. Sample at 250 μM were also injected in mixture with 10 μM *d*-tubocurarine. Data analysis for the dose–response experiments was performed similarly as described above. Apparent affinities were determined by nonlinear regression analysis of dose–response data obtained at the Binding Early report points from reference-subtracted sensorgrams using the Sprint software (Beactica AB), accounting for nonspecific binding.

Electrophysiological Recordings. All experiments were carried out on human α7 nAChRs expressed in *Xenopus* oocytes using the method of cDNA or cRNA expression, as described before (38). All mutant receptors were constructed using a QuikChange strategy and verified by sequencing. cRNA was synthesized using the T7 mMESSAGE-mMACHINE transcription kit (Ambion). *Xen-*

opus oocytes were prepared and injected using standard procedures. Briefly, ovaries were harvested from *Xenopus laevis* females that have been deeply anesthetized by cooling at 4 °C and with MS-222 (150 mg/L). Once anesthetized the animal was decapitated following the rules of animal rights from the Geneva canton. A small piece of ovary was isolated for immediate preparation and the remaining part was placed at 4 °C in a sterile Barth solution containing (in millimolar) NaCl 88, KCl 1, NaHCO$_3$ 2.4, Hepes 10, MgSO$_4^0$·7 H$_2$O 0.82, Ca(NO$_3$)$_2$·4 H$_2$O 0.33, CaCl$_2^0$·6 H$_2$O 0.41 (pH 7.4), and supplemented with 20 μg/mL of kanamycine, 100 units/mL penicillin, and 100 μg/mL streptomycin.

Injections of WT α7 nAChR cDNA and mutant α7 nAChR cRNA were performed in ≥100 oocytes using a proprietary automated injection device. Receptor expression was examined at least 2 d later.

Oocytes were impaled with two electrodes and their membrane potential maintained at −80 mV throughout the experiment. ACh was prepared as a concentrated stock solution (100 μM) in water and diluted in the recording medium to obtain the desired test concentration. Fragments were prepared as stock solutions in DMSO and diluted to the desired concentrations immediately before the experiment. All recordings were performed at 18 °C and cells were superfused with OR2 medium containing (in millimolar) NaCl 82.5, KCl 2.5, Hepes 5, CaCl$_2$·2 H$_2$O 1.8, MgCl$_2$·6 H$_2$O 1 (pH 7.4). Currents evoked by ACh were recorded using an automated process equipped with standard two-electrode voltage clamp configuration. Data were captured and analyzed using a HiQScreen proprietary data acquisition and analysis software running under MATLAB (The MathWorks, Inc.). All experiments were carried out using at least three cells and statistical analysis was preformed either with Excel (Microsoft) or MATLAB. Plots of the peak inward currents as a function of the logarithm of the agonist concentration yield classical concentration-activation and concentration-inhibition curves that are readily fitted by single Hill equations.

1. Wallace TL, Porter RHP (2011) Targeting the nicotinic alpha7 acetylcholine receptor to enhance cognition in disease. *Biochem Pharmacol* 82(8):891–903.
2. Taly A, Corringer P-J, Guedin D, Lestage P, Changeux J-P (2009) Nicotinic receptors: Allosteric transitions and therapeutic targets in the nervous system. *Nat Rev Drug Discov* 8(9):733–750.
3. Brams M, et al. (2011) A structural and mutagenic blueprint for molecular recognition of strychnine and d-tubocurarine by different cys-loop receptors. *PLoS Biol* 9(3):e1001034.
4. Bertrand D, Gopalakrishnan M (2007) Allosteric modulation of nicotinic acetylcholine receptors. *Biochem Pharmacol* 74(8):1155–1163.
5. Du J, Dong H, Zhou H-X (2012) Size matters in activation/inhibition of ligand-gated ion channels. *Trends Pharmacol Sci* 33(9):482–493.
6. Bourne Y, Talley TT, Hansen SB, Taylor P, Marchot P (2005) Crystal structure of a Cbtx-AChBP complex reveals essential interactions between snake alpha-neurotoxins and nicotinic receptors. *EMBO J* 24(8):1512–1522.
7. Brejc K, et al. (2001) Crystal structure of an ACh-binding protein reveals the ligand-binding domain of nicotinic receptors. *Nature* 411(6835):269–276.
8. Hansen SB, et al. (2005) Structures of Aplysia AChBP complexes with nicotinic agonists and antagonists reveal distinctive binding interfaces and conformations. *EMBO J* 24(20):3635–3646.
9. Celie PHN, et al. (2004) Nicotine and carbamylcholine binding to nicotinic acetylcholine receptors as studied in AChBP crystal structures. *Neuron* 41(6):907–914.
10. Hibbs RE, et al. (2009) Structural determinants for interaction of partial agonists with acetylcholine binding protein and neuronal alpha7 acetylcholine receptor. *EMBO J* 28(19):3040–3051.
11. Hibbs RE, Gouaux E (2011) Principles of activation and permeation in an anion-selective Cys-loop receptor. *Nature* 474(7349):54–60.
12. Bocquet N, et al. (2009) X-ray structure of a pentameric ligand-gated ion channel in an apparently open conformation. *Nature* 457(7225):111–114.
13. Hilf RJC, Dutzler R (2009) Structure of a potentially open state of a proton-activated pentameric ligand-gated ion channel. *Nature* 457(7225):115–118.
14. Hilf RJC, Dutzler R (2008) X-ray structure of a prokaryotic pentameric ligand-gated ion channel. *Nature* 452(7185):375–379.
15. Smit AB, et al. (2001) A glia-derived acetylcholine-binding protein that modulates synaptic transmission. *Nature* 411(6835):261–268.
16. Celie PHN, et al. (2005) Crystal structure of nicotinic acetylcholine receptor homolog AChBP in complex with an alpha-conotoxin PnIA variant. *Nat Struct Mol Biol* 12(7):582–588.
17. Pan J, et al. (2012) Structure of the pentameric ligand-gated ion channel GLIC bound with anesthetic ketamine. *Structure* 20(9):1463–1469.
18. Sieghart W (1995) Structure and pharmacology of gamma-aminobutyric acidA receptor subtypes. *Pharmacol Rev* 47(2):181–234.
19. Timmermann DB, et al. (2007) An allosteric modulator of the alpha7 nicotinic acetylcholine receptor possessing cognition-enhancing properties in vivo. *J Pharmacol Exp Ther* 323(1):294–307.
20. Spurny R, et al. (2012) Pentameric ligand-gated ion channel ELIC is activated by GABA and modulated by benzodiazepines. *Proc Natl Acad Sci USA* 109(44):E3028–E3034.
21. Hurst RS, et al. (2005) A novel positive allosteric modulator of the alpha7 neuronal nicotinic acetylcholine receptor: In vitro and in vivo characterization. *J Neurosci* 25(17):4396–4405.
22. Bertrand D, et al. (2008) Positive allosteric modulation of the alpha7 nicotinic acetylcholine receptor: Ligand interactions with distinct binding sites and evidence for a prominent role of the M2-M3 segment. *Mol Pharmacol* 74(5):1407–1416.
23. Li S-X, et al. (2011) Ligand-binding domain of an α7-nicotinic receptor chimera and its complex with agonist. *Nat Neurosci* 14(10):1253–1259.
24. Violet JM, Downie DL, Nakisa RC, Lieb WR, Franks NP (1997) Differential sensitivities of mammalian neuronal and muscle nicotinic acetylcholine receptors to general anesthetics. *Anesthesiology* 86(4):866–874.
25. Nury H, et al. (2011) X-ray structures of general anaesthetics bound to a pentameric ligand-gated ion channel. *Nature* 469(7330):428–431.
26. Zuo Y, et al. (2001) Dual action of n-alcohols on neuronal nicotinic acetylcholine receptors. *Mol Pharmacol* 60(4):700–711.
27. Jenkins A, et al. (2008) General anesthetics have additive actions on three ligand gated ion channels. *Anesth Analg* 107(2):486–493.
28. Sauguet L, et al. (2013) Structural basis for potentiation by alcohols and anaesthetics in a ligand-gated ion channel. *Nat Commun* 4:1697.
29. Zhang JH, Chung TD, Oldenburg KR (1999) A simple statistical parameter for use in evaluation and validation of high throughput screening assays. *J Biomol Screen* 4(2):67–73.
30. Krause RM, et al. (1998) Ivermectin: A positive allosteric effector of the alpha7 neuronal nicotinic acetylcholine receptor. *Mol Pharmacol* 53(2):283–294.
31. Harrison NL, Simmonds MA (1985) Quantitative studies on some antagonists of N-methyl D-aspartate in slices of rat cerebral cortex. *Br J Pharmacol* 84(2):381–391.
32. Coates KM, Flood P (2001) Ketamine and its preservative, benzethonium chloride, both inhibit human recombinant alpha7 and alpha4beta2 neuronal nicotinic acetylcholine receptors in Xenopus oocytes. *Br J Pharmacol* 134(4):871–879.
33. Kabsch W (2010) XDS. *Acta Crystallogr D Biol Crystallogr* 66(Pt 2):125–132.
34. Winn MD, et al. (2011) Overview of the CCP4 suite and current developments. *Acta Crystallogr D Biol Crystallogr* 67(Pt 4):235–242.
35. Adams PD, et al. (2010) PHENIX: A comprehensive Python-based system for macromolecular structure solution. *Acta Crystallogr D Biol Crystallogr* 66(Pt 2):213–221.
36. Emsley P, Lohkamp B, Scott WG, Cowtan K (2010) Features and development of Coot. *Acta Crystallogr D Biol Crystallogr* 66(Pt 4):486–501.
37. Chen VB, et al. (2010) MolProbity: All-atom structure validation for macromolecular crystallography. *Acta Crystallogr D Biol Crystallogr* 66(Pt 1):12–21.
38. Hogg RC, Bandelier F, Benoit A, Dosch R, Bertrand D (2008) An automated system for intracellular and intranuclear injection. *J Neurosci Methods* 169(1):65–75.